

# Quantum Approximate Optimization with a Trapped-Ion Quantum Simulator

G. Pagano<sup>1</sup>, A. Bapat<sup>1</sup>, P. Becker<sup>1</sup>, K. S. Collins<sup>1</sup>, A. De<sup>1</sup>, P. W. Hess<sup>1,2</sup>, H. B. Kaplan<sup>1</sup>, A. Kyprianidis<sup>1</sup>, W. L. Tan<sup>1</sup>, C. Baldwin<sup>1</sup>, L. T. Brady<sup>1</sup>, A. Deshpande<sup>1</sup>, F. Liu<sup>1</sup>, S. Jordan<sup>3</sup>, A. V. Gorshkov<sup>1</sup>, and C. Monroe<sup>1</sup>

<sup>1</sup> *Joint Quantum Institute, Joint Center for Quantum Information and Computer Science, and Physics Department, University of Maryland and National Institute of Standards and Technology, College Park, MD 20742*

<sup>2</sup> *Middlebury College Department of Physics, Middlebury, VT 05753, USA and*

<sup>3</sup> *University of Maryland Institute for Advanced Computer Studies, College Park, Maryland 20742, USA*

Quantum computers and simulators may offer significant advantages over their classical counterparts, providing insights into quantum many-body systems [1] and possibly solving exponentially hard problems [2], such as optimization [3] and satisfiability [4]. Here we report the first implementation of a shallow-depth Quantum Approximate Optimization Algorithm (QAOA) [5] using an analog quantum simulator to estimate the ground state energy of the transverse field Ising model with tunable long-range interactions. First, we exhaustively search the variational control parameters to approximate the ground state energy with up to 40 trapped-ion qubits. We then interface the quantum simulator with a classical algorithm to more efficiently find the optimal set of parameters that minimizes the resulting energy of the system. We finally sample from the full probability distribution of the QAOA output with single-shot and efficient measurements of every qubit.

It remains an open question whether quantum computers or simulators can efficiently solve classically hard combinatorial problems. One possible approach is to use quantum devices to perform quantum annealing [3, 6], which in some cases may provide an advantage over classical approaches [7, 8]. However, quantum annealing has stringent adiabaticity requirements that hinder its applicability on existing quantum platforms that have finite coherence times [9].

Alternatively, hybrid quantum-classical variational algorithms may approximately solve hard problems in realms such as quantum magnetism, quantum chemistry [10], and high-energy physics [11]. This is because the key resource of quantum computers and simulators is quantum entanglement, which is exactly what makes these many-body quantum problems hard. In a hybrid variational algorithm, entangled states are functions of variational parameters that are iteratively optimized by a classical algorithm. One example is the Quantum Approximate Optimization Algorithm [5], which consists of a “bang-bang” protocol that can provide an approximate answer in a time-efficient way, using devices with finite coherence times and without the use of error-correction [12, 13].

Similarly to quantum annealing, the QAOA protocol encodes the objective function of the optimization problem in a target spin Hamiltonian. The optimization steps of the QAOA are based on unitary evolution under the target Hamiltonian and a non commuting “mixing” operator. The QAOA is theoretically motivated from complexity theory [14, 15] and optimal control theory [10, 16, 17], and may be seen more intuitively as replacing infinitesimal (Trotterized) Hamiltonian time evolution by an appropriate sequence of finite time steps. The QAOA relies on a classical outer loop to optimize the quantum circuit, aided by physical intuition [17, 18] or observed

structure of the variational parameters [13, 19, 20], producing fast, low-depth circuits for approximate solutions.

In this work, we employ a collection of interacting trapped-ion qubits to experimentally implement a specific instance of the QAOA. We focus on the energy minimization of a transverse field anti-ferromagnetic Ising Hamiltonian with long-range interactions [21]:

$$H = \underbrace{\sum_{i<j} J_{ij} \sigma_i^x \sigma_j^x}_{H_A} + B \underbrace{\sum_i \sigma_i^y}_{H_B}. \quad (1)$$

Here we set Planck’s constant  $\hbar = 1$ ,  $\sigma_i^\gamma$  ( $\gamma = x, y, z$ ) is the Pauli matrix acting on the  $i^{\text{th}}$  spin along the  $\gamma$  direction of the Bloch sphere,  $J_{ij} > 0$  is the Ising coupling between spins  $i$  and  $j$ , and  $B$  denotes the transverse magnetic field. It is well-known [22] that the Hamiltonian (1) exhibits a quantum phase transition for anti-ferromagnetic interactions with power law decay. One of the goals of this work is to find an approximation of the ground state energy at the critical point  $(B/J_0)_c$ , where  $J_0$  is the average nearest-neighbour coupling. In this case, the realization of the QAOA entails a series of unitary quantum evolutions (see Fig. 1) under the non-commuting Hamiltonians  $H_A$  and  $H_B$  that are applied to a known initial state  $|\psi_0\rangle$ . The state obtained after  $p$  layers of the QAOA is:

$$|\vec{\beta}, \vec{\gamma}\rangle = \prod_{k=1}^p e^{-i\beta_k(H_B/J_0)} e^{-i\gamma_k(H_A/J_0)} |\psi_0\rangle, \quad (2)$$

where the angles  $\beta_k$  and  $\gamma_k$  are variational parameters used in the  $k$ -th QAOA layer to minimize the final energy  $E(\vec{\beta}, \vec{\gamma}) = \langle \vec{\beta}, \vec{\gamma} | H | \vec{\beta}, \vec{\gamma} \rangle$ .

In order to implement the quantum optimization algorithm, each spin in the chain is encoded in the  $^2S_{1/2}$

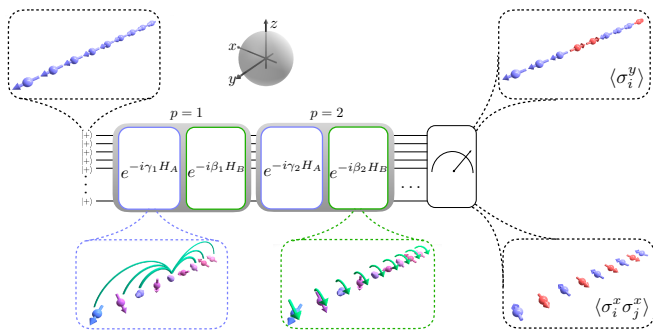


**Figure 1: QAOA protocol.** The system is initialized along the  $y$  direction in the Bloch sphere in the  $|+\rangle^{\otimes N}$  state. The unitary evolution under  $H_{A(B)}$  is implemented for angles  $\gamma_i(\beta_i)$  for  $p$  times. At the end of the algorithm global measurements in the  $x$  and the  $y$  basis are performed to compute the average energy  $\langle H \rangle = E(\vec{\beta}, \vec{\gamma})$ , which is compared to the theoretical ground state energy  $E_{gs}$ .

$|F = 0, m_F = 0\rangle \equiv |\downarrow\rangle_z$  and  $|F = 1, m_F = 0\rangle \equiv |\uparrow\rangle_z$  hyperfine “clock” states of a  $^{171}\text{Yb}^+$  ion (see Methods). In this work, depending on the number of qubits and measurements required, we employ two different quantum simulation apparatus to run the QAOA, which will herein be referred to as system 1 [23] and system 2 [24] (see Methods). Both systems are based on a linear rf Paul trap where we store chains of up to  $N = 40$  ions and initialize the qubits in the ground state of  $H_B$ , namely the product state  $|\uparrow\uparrow \dots \uparrow\rangle_y \equiv |+\rangle^{\otimes N} = |\psi_0\rangle$ , where  $|\uparrow\rangle_y \equiv (|\uparrow\rangle_z + i|\downarrow\rangle_z)/\sqrt{2}$  and  $B$  is assumed to be negative. The unitary evolution under  $H_A$  is realized by generating spin-spin interactions through spin-dependent optical dipole forces implemented by an applied laser field. This gives rise to effective tunable long-range Ising couplings that fall off approximately as  $J_{ij} \approx J_0/|i-j|^\alpha$  [25]. The power-law exponent  $\alpha \sim 1$  and the interaction strengths vary in the range  $J_0/2\pi = (0.3-0.57)$  kHz, depending on the system size and the experimental realization (see Methods for details). The unitary evolution under  $H_B$  is generated by applying a global rotation around the  $y$ -axis of the Bloch sphere.

After each run of the algorithm, we perform a projective measurement of each spin in the  $x(y)$  basis to measure  $\langle H_A \rangle$  ( $\langle H_B \rangle$ ) (see Fig. 1). Measurements in the  $x$  and  $y$  bases are carried out by performing a  $\pi/2$  rotation about the  $y(x)$ -axis of the Bloch sphere, illuminating the ions with resonant laser light, and collecting the  $\sigma_i^z$ -dependent fluorescence on a camera with site-resolved imaging. The energy is calculated by combining the measurements of the two-body correlators  $\langle \sigma_i^x \sigma_j^x \rangle$  and the total magnetization along the  $y$  axis  $\sum_i \langle \sigma_i^y \rangle$ , where the indices  $i, j$  range from 1 to  $N$ . We benchmark the experimental outcome  $E(\vec{\beta}, \vec{\gamma})$  with the ground state  $E_{gs}$  of the target Hamiltonian (see Eq. 1) calculated numerically with exact diagonalization or Density Matrix Renormalization Group (DMRG) [26]. In order to quan-

tify the performance of the QAOA, we use the dimensionless quantity

$$\eta \equiv \frac{E(\vec{\beta}, \vec{\gamma}) - E_{max}}{E_{gs} - E_{max}}, \quad (3)$$

where  $E_{max}$  is the energy of the highest excited state. This choice maps the entire many-body spectrum to the  $[0, 1]$  interval. In the following we show that the best experimental performance  $\eta^*$  is close to the theoretical performance  $\eta_{th}$ , which itself is less than unity for a finite number  $p$  of QAOA layers.

We first focus on the  $p = 1$  case, where only two variational parameters ( $\gamma$  and  $\beta$ ) are used to minimize the energy. In this case, the time-evolved one- and two-point correlation functions can be efficiently computed [27]. This leads to a general formula for the energy expectation under a state produced by the  $p = 1$  QAOA that is used to compute the theoretical performance of the algorithm (see Methods). In Fig. 2a we show an experimental exhaustive search over the parameter space  $\{\gamma, \beta\}$  and compare it to the theoretical performance of the algorithm, showing good agreement for  $N = 20$  qubits. We also compare the performance of our algorithm as a function of  $B/J_0$  with the expected QAOA performance  $\eta_{th}$  (see Fig. 2b).

As shown in Ref. [22], for transverse field greater than the critical value, the ground state is a low entanglement paramagnet, whereas below the critical point the ground state is an entangled superposition of anti-ferromagnetic states. We locate this critical point at  $|B/J_0| = 0.31$  for 20 qubits by computing the half-chain entanglement entropy  $S_{L/2} = -\text{Tr}(\rho_{L/2} \log \rho_{L/2})$  of the ground state numerically. As shown in Fig. 2b, while the experimental performance is  $\eta > 94\%$  when  $|B/J_0|$  is above the critical point, the gain relative to the initial state  $|\psi_0\rangle$  is modest. On the other hand, below the critical point, the target state is more entangled, which allows for a larger experimental performance gain, at the expense of a reduced absolute performance.

We investigate the performance of the  $p = 1$  QAOA algorithm as a function of the number of qubits. For each system size, we ensure that the spin-spin couplings  $J_{ij}$  have the same dependence on the qubit distance  $|i-j|$  by varying the trap parameters (see Methods). As shown in Fig. 2c, the half-chain entanglement entropy as a function of system size  $N$  exhibits a peak located at  $B/J_0 \sim -0.33$ , displaying the onset of the phase transition as  $N$  tends to infinity. For all system sizes, we optimize the algorithm by performing a scan of the interaction angle  $\gamma$  and applying discrete variations of the mixing angle  $\beta$  around the optimal value predicted by the theory. In Fig. 2c we compare the optimal experimental and theoretical performances  $\eta$  for different system sizes from 20 up to 40 qubits for fixed  $B/J_0 \sim -0.3$ . We conclude from both the numerics and experimental data that

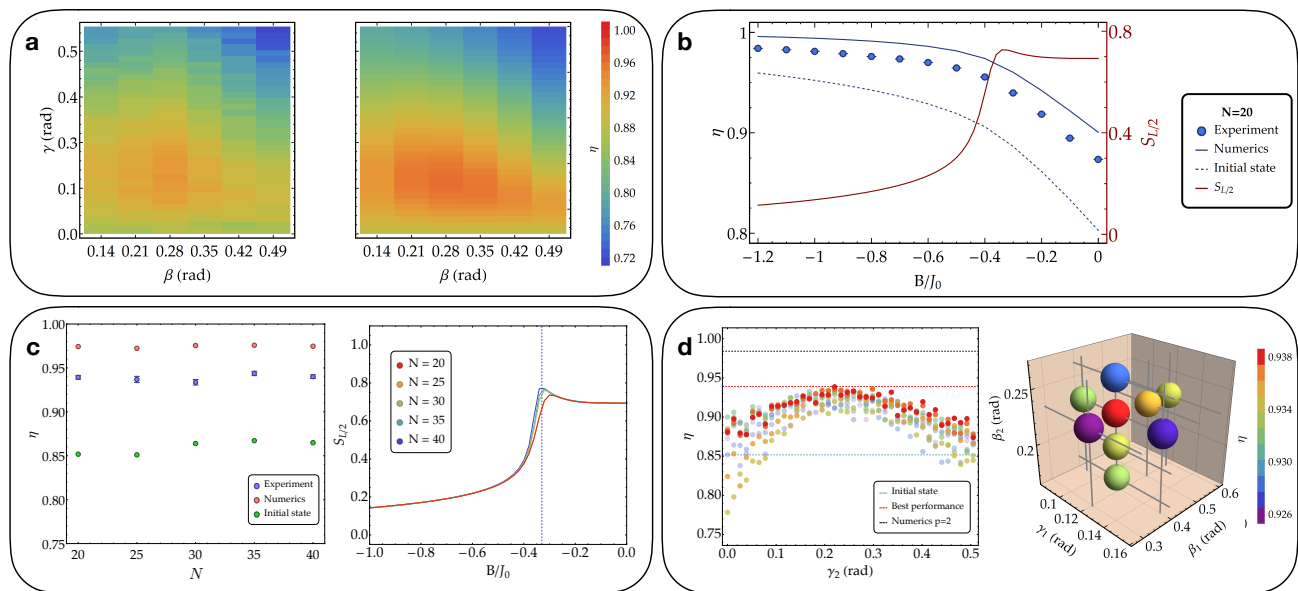


**Figure 2: Exhaustive search for optimal performance.** (a) Experimental (left) and theoretical (right) energy landscape as a function of the variational parameters  $\beta$  and  $\gamma$  for  $N = 20$  qubits ( $J_0/2\pi = 0.57$  kHz,  $B/J_0 \sim -0.3$ ). The optimal performance is  $\eta^* = (93.8 \pm 0.4)\%$ , whereas the theoretical performance is  $\eta_{th} = 96.1\%$ . Each data point is the result of 1100 (800) experimental repetitions to measure in the  $x$  ( $y$ ) basis (data taken on system 1). (b) Exhaustive search optimization as a function of  $B/J_0$  (see Eq. (1)). The error bars are calculated by using the standard deviation from the mean of the measured energy (data taken on system 1). The dark red solid line is the half-chain entanglement entropy  $S_{L/2}$  computed numerically with DMRG. The dashed blue line represents the performance of the initial product state  $|\psi_0\rangle$ . (c) Left: comparison between QAOA experimental and theoretical performance for  $B/J_0 \sim -0.3$ . Green points show the baseline performance of the initial state  $|\psi_0\rangle$ . Right: Convergence of the entanglement entropy peak as a function of number of qubits (see Methods). (d)  $p = 2$  exhaustive search for  $N = 20$  and  $B/J_0 = -0.3$ . Left: every color corresponds to a fine scan of  $\gamma_2$  with a different set of variational parameters  $\beta_1, \beta_2$  and  $\gamma_1$  (data taken on system 2). Right: 3D color plot of the performance  $\eta$ , optimized over  $\gamma_2$ , as a function of the parameters  $\beta_1, \beta_2$  and  $\gamma_1$ . The best outcome is  $\eta^* = (93.9 \pm 0.3)\%$  (colored red), whereas the theoretical performance is  $\eta_{th} = 98.4\%$  (see main text for details).

the QAOA yields a similar performance as a function of number of qubits, even if the algorithm runtime changes negligibly as the number of qubits increases.

We experimentally perform a search for the optimal  $p = 2$  QAOA performance using 20 qubits. Unlike the  $p = 1$  case, there is no known analytic formula to efficiently compute the energy. However, exploiting relationships between optimal angles as a function of increasing  $p$ , we use a bootstrapping heuristic (see Methods for details) that allows the experiment to identify a set of optimal angles faster than a global parameter search. We start from the optimal guess and perform a fine scan of  $\gamma_2$ , while varying  $\gamma_1, \beta_1$  and  $\beta_2$  in larger steps. The result is shown in Fig. 2d, where we plot the performances  $\eta$  as a function of  $\gamma_2$  for every set of parameters used in the experiment. Fig. 2d shows also a colour plot of all the optimal energies found as a function of the other three parameters  $\gamma_1, \beta_1$  and  $\beta_2$ . The  $p = 2$  QAOA performance with 20 qubits  $\eta^* = (93.9 \pm 0.3)\%$  is in agreement with the  $p = 1$  performance in system 2, taken with the same parameters (see Fig. 2c). This indicates that decoherence and bit-flip errors (see Methods) accumulated

during longer evolution times are already balancing out the 2% expected performance gain of one additional optimization layer.

As a brute force approach is inefficient, we implement a closed-loop QAOA by interfacing the analog trapped-ion quantum simulator with a greedy gradient-descent algorithm to optimize the measured energy. In the  $p = 1$  QAOA, we can visualize the optimization trajectory on the theoretical performance surface as shown in Fig. 3. The procedure goes as follows: (i) we start from a guess  $(\beta^{(0)}, \gamma^{(0)})$  and measure its energy. (ii) We measure the approximate local gradient by performing the energy measurements in two orthogonal directions  $\beta^{(0)} + \delta\beta$  and  $\gamma^{(0)} + \delta\gamma$ . (iii) The algorithm computes the new guess  $(\beta^{(1)}, \gamma^{(1)})$ . The new energy is then measured on the quantum simulator. Steps (ii) - (iii) are iterated until convergence of the algorithm. As shown in Fig. 3, the algorithm converges after about 10 iterations. Compared to an exhaustive search, the gradient descent uses a fewer number of queries to the quantum simulator and is therefore more robust to slow drifts in the experimental system. For this reason, we are able to achieve a better

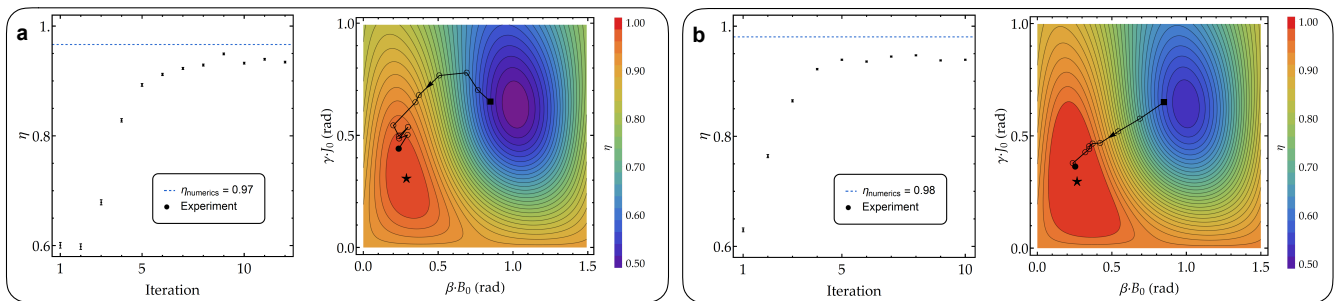


**Figure 3: Gradient descent search for  $p=1$  QAOA.** (a)  $N = 12$  and (b)  $N = 20$ . Left: performance  $\eta$  convergence as a function of iterations of the classical-quantum hybrid algorithm with (a)  $N = 12$  ( $J_0/2\pi = 0.57$  kHz,  $B/J_0 = -0.3$ ) with a measured  $\eta^* = (94.9 \pm 0.2)\%$  and (b)  $N = 20$  qubits ( $J_0/2\pi = 0.55$  kHz,  $B/J_0 = -0.3$ ) with a measured  $\eta^* = (94.7 \pm 0.1)\%$ . Right: the algorithm trajectory on the theoretical performance landscape plotted as a function of  $\gamma$  and  $\beta$ . Each energy evaluation takes 4000 (6000) shots for 12 (20) qubits. The error bars are standard deviation from the mean of the measured performance (data taken on system 1).

performance compared to the exhaustive search method.

We further explore the performance of our system by investigating higher-order observables in the output of the  $p = 1$  QAOA, using high-fidelity single-shot measurement of all the qubits. It has been proven, under reasonable complexity-theoretic assumptions, that no classical algorithm can efficiently sample exactly from a sufficiently general class of  $p = 1$  QAOA circuits [14]. Recent results [28, 29] suggest that this could also hold in the case of approximate sampling (see Methods). In order to approximately sample from the QAOA, we optimize the algorithm to solve for the ground state of  $H_A$  alone (see Eq. (1)), namely in the absence of a transverse field. In this case, by measuring in the  $x$  basis, it is possible to sample the probability distribution of all the  $2^N$  eigenstates  $|x_i\rangle$  of the Hamiltonian  $H_A$ . We performed the experiment with 12 qubits so that we can both compute the expected QAOA theoretical output and also experimentally over-sample the Hilbert space of all the possible  $2^{12} = 4096$  possible outcomes. In Fig. 4a we show the raw QAOA outcome using the optimal variational parameters  $\beta^*$ ,  $\gamma^*$  and compare the experimental eigenstate histogram with the exact diagonalization prediction of the QAOA output state, showing qualitative agreement.

However, sampling from the full QAOA output distribution is a daunting task, since the experimental outcome is extremely sensitive to fluctuations in the Hamiltonian parameters and to experimental errors caused by detection and phonon-assisted bit-flip events (see Methods). We can take into account these errors by implementing the coarse-graining procedure of the Hilbert space proposed in Ref. [30]. After sorting in decreasing order the observed states according to their experimental probability, we iteratively group the states into “bubbles” of Hamming distance  $L$  around the most probable state, producing a coarse-grained dataset. We then apply the same coarse-graining to the theoretical probability distribution and plot the comparison in Fig. 4b. In this

procedure the Hamming distance radius is varied to ensure that each bubble contains a comparable number of experimental shots, leading to bubbles of average Hamming distance  $\bar{L} = 2.5$ .

In order to quantitatively compare the coarse-grained experiment and the theory, we estimate two different metrics, namely the total variation distance (TVD) and the Kullback-Leibler divergence ( $D_{K-L}$ ), defined as:

$$\text{TVD} = \frac{1}{2} \sum_i |p_i - q_i|, \quad (4)$$

$$D_{K-L} = - \sum_i p_i \log \left( \frac{q_i}{p_i} \right), \quad (5)$$

where  $p_i$  ( $q_i$ ) is the experimental (theoretical) probability of observing the  $i$ -th outcome. As shown in Fig. 4c, when the system is in the initial state, it is closer to a uniform probability distribution since  $|\psi_0\rangle$  is an equal superposition of all the eigenstates of  $H_A$ . On the other hand, as the  $\gamma$  parameter is scanned, we observe a net decrease of both TVD and  $D_{K-L}$ , in agreement with the decrease in energy, computed by measuring one and two-body correlators.

The variational quantum algorithm reported here, with up to 40 trapped-ion qubits, is the largest ever realized on a quantum device. We approximate the ground state energy of a non-trivial quantum Hamiltonian showing almost constant time scaling with the system size. Single-shot high-efficiency qubit measurements in different bases give access to the full distribution of bit-strings that is difficult or potentially impossible to model classically. With the addition of individual control over the interactions between qubits, the variational quantum-classical hybrid approach can be employed in this experimental platform to give insight into quantum chemistry [31–33] and hard optimization problems, such as Max-SAT or exact cover [4], or be used for the production of highly entangled states of metrological interest [34].

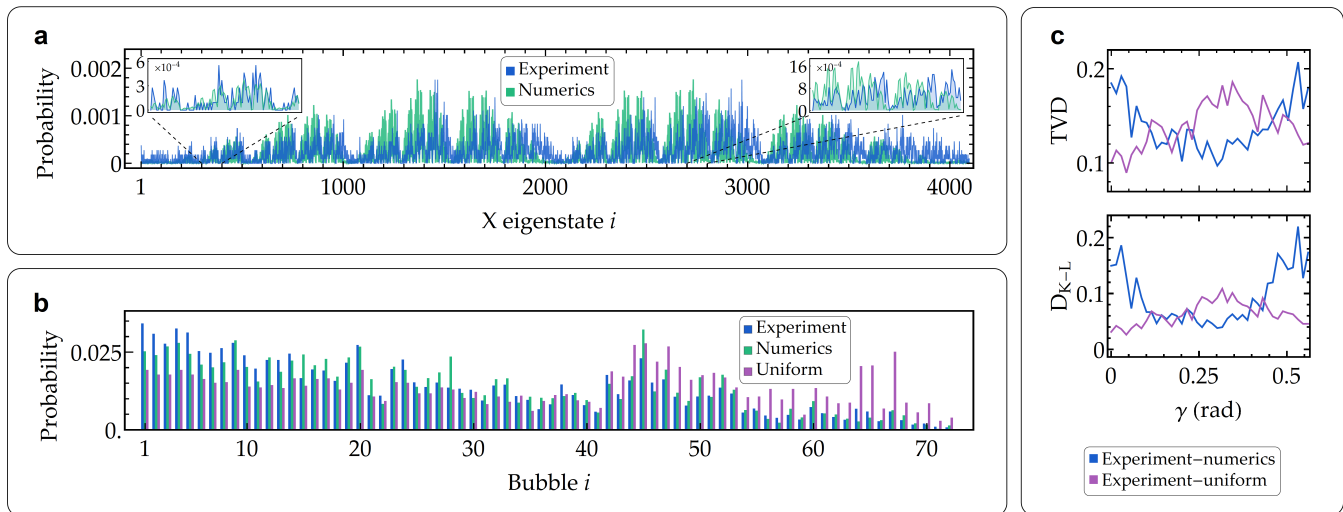


**Figure 4: Sampling from  $p = 1$  QAOA.** (a) State histogram for 12 qubits with  $B = 0$  and  $J_0/2\pi = 0.45$  kHz. The numerical histogram is computed by decomposing the ideal QAOA output state on the  $\{|x_i\rangle\}$  basis. We performed 10800 measurements at the optimal parameters  $\beta^*$  and  $\gamma^*$  to oversample the Hilbert space of dimension  $2^N = 4096$ . (b) Histogram of coarse-grained distributions (see main text for details) comparing data, theory and the uniform distribution. (c) Total Variation Distance and Kullback-Leibler divergence as a function of  $\gamma$ , keeping  $\beta$  fixed at the optimal value. The distance from the uniform distribution increases as the  $\gamma$  parameter reaches the optimal point  $\gamma^*$  (data taken on system 2).

### Acknowledgements

We acknowledge illuminating discussions with L. Duan, Y. Wu, B. Fefferman and S. Wang. The DMRG simulations were performed using Open Source Matrix Product States [26]. This work is supported by the ARO and AFOSR QIS and Atomic and Molecular Physics Programs, the AFOSR MURIs on Quantum Measurement/Verification and Quantum Interactive Protocols, the IARPA LogiQ program, the ARO MURI on Modular Quantum Systems, the ARL Center for Distributed Quantum Information, the NSF QIS program, the NSF PFCQC Program, the DOE BES QIS Program, the DOE HEP QuantISED Program, the DOE ASCR Quantum Testbed Pathfinder and Quantum Algorithms Teams (QOALAs) programs, and the NSF Physics Frontier Center at JQI.

### Author Contributions

G.P., A.K., P.B., W.L.T., H.B.K., K.S.C., A.D., P.W.H. and C.M. all contributed to experimental design, construction, data collection and analysis. A.B., L.T.B., F.L., A.D., C.B., S.J. and A.V.G. contributed to the theory for the experiment. All authors contributed to this manuscript.

### Author Information

The authors declare competing financial interests: details are available in the online version of the paper. Readers are welcome to comment on the online version of the paper. Correspondence and requests for materials should be addressed to G.P. (pagano@umd.edu)

- 
- [1] Feynman, R. P. Simulating physics with computers. *International Journal of Theoretical Physics* **21**, 467–488 (1982).
  - [2] Nielsen, M. A. & Chuang, I. L. *Quantum Computation and Quantum Information: 10th Anniversary Edition* (Cambridge University Press, New York, NY, USA, 2011), 10th edn.
  - [3] Farhi, E., Goldstone, J., Gutmann, S. & Sipser, M. Quantum Computation by Adiabatic Evolution. *arXiv e-prints* quant-ph/0001106 (2000). quant-ph/0001106.
  - [4] Farhi, E. *et al.* A quantum adiabatic evolution algorithm applied to random instances of an np-complete problem. *Science* **292**, 472–475 (2001).
  - [5] Farhi, E., Goldstone, J. & Gutmann, S. A Quantum Approximate Optimization Algorithm. *arXiv e-prints* arXiv:1411.4028 (2014). 1411.4028.
  - [6] Kadowaki, T. & Nishimori, H. Quantum annealing in the transverse Ising model. *Phys. Rev. E* **58**, 5355–5363 (1998). cond-mat/9804280.
  - [7] Santoro, G. E., Martoňák, R., Tosatti, E. & Car, R. Theory of quantum annealing of an ising spin glass. *Science* **295**, 2427–2430 (2002).
  - [8] Hastings, M. B. & Freedman, M. H. Obstructions To



- Classically Simulating The Quantum Adiabatic Algorithm. *arXiv e-prints* arXiv:1302.5733 (2013). 1302.5733.
- [9] Richerme, P. *et al.* Experimental performance of a quantum simulator: Optimizing adiabatic evolution and identifying many-body ground states. *Phys. Rev. A* **88**, 012334 (2013).
- [10] McClean, J. R., Romero, J., Babbush, R. & Aspuru-Guzik, A. The theory of variational hybrid quantum-classical algorithms. *New Journal of Physics* **18**, 023023 (2016).
- [11] Kokail, C. *et al.* Self-Verifying Variational Quantum Simulation of the Lattice Schwinger Model. *arXiv e-prints* arXiv:1810.03421 (2018). 1810.03421.
- [12] Preskill, J. Quantum Computing in the NISQ era and beyond. *Quantum* **2**, 79 (2018).
- [13] Zhou, L., Wang, S.-T., Choi, S., Pichler, H. & Lukin, M. D. Quantum Approximate Optimization Algorithm: Performance, Mechanism, and Implementation on Near-Term Devices. *arXiv e-prints* arXiv:1812.01041 (2018). 1812.01041.
- [14] Farhi, E. & Harrow, A. W. Quantum supremacy through the quantum approximate optimization algorithm. *arXiv preprint arXiv:1602.07674* (2016).
- [15] Lloyd, S. Quantum approximate optimization is computationally universal. *arXiv e-prints* arXiv:1812.11075 (2018). 1812.11075.
- [16] Yang, Z. C., Rahmani, A., Shabani, A., Neven, H. & Chamon, C. Optimizing variational quantum algorithms using pontryagin’s minimum principle. *Physical Review X* **7**, 1–8 (2017). 1607.06473.
- [17] Bapat, A. & Jordan, S. Bang-bang control as a design principle for classical and quantum optimization algorithms. *arXiv preprint arXiv:1812.02746* (2018).
- [18] Verdon, G., Pye, J. & Broughton, M. A universal training algorithm for quantum deep learning. *arXiv preprint arXiv:1806.09729* (2018).
- [19] Brady, L., Bapat, A. & Gorshkov, A. *in preparation* (2019).
- [20] Crooks, G. E. Performance of the quantum approximate optimization algorithm on the maximum cut problem. *arXiv preprint arXiv:1811.08419* (2018).
- [21] Zhang, J. *et al.* Observation of a many-body dynamical phase transition with a 53-qubit quantum simulator. *Nature* **551**, 601–604 (2017).
- [22] Koffel, T., Lewenstein, M. & Tagliacozzo, L. Entanglement entropy for the long-range ising chain in a transverse field. *Physical Review Letters* **109** (2012).
- [23] Kim, K. *et al.* Entanglement and tunable spin-spin couplings between trapped ions using multiple transverse modes. *Physical Review Letters* **103** (2009).
- [24] Pagano, G. *et al.* Cryogenic trapped-ion system for large scale quantum simulation. *Quantum Science and Technology* **4**, 014004 (2019).
- [25] Porras, D. & Cirac, J. I. Effective Quantum Spin Systems with Trapped Ions. *Phys. Rev. Lett.* **92**, 207901 (2004).
- [26] Jaschke, D., Wall, M. L. & Carr, L. D. Open source matrix product states: Opening ways to simulate entangled many-body quantum systems in one dimension. *Computer Physics Communications* **225**, 59 – 91 (2018).
- [27] Dylewsky, D., Freericks, J., Wall, M., Rey, A. & Foss-Feig, M. Nonperturbative calculation of phonon effects on spin squeezing. *Physical Review A* **93**, 013415 (2016).
- [28] Bremner, M. J., Montanaro, A. & Shepherd, D. J. Average-case complexity versus approximate simulation of commuting quantum computations. *Phys. Rev. Lett.* **117**, 080501 (2016).
- [29] Bouland, A., Fefferman, B., Nirkhe, C. & Vazirani, U. On the complexity and verification of quantum random circuit sampling. *Nat. Phys.* **15**, 159–163 (2019).
- [30] Wang, S.-T. & Duan, L.-M. Certification of Boson Sampling Devices with Coarse-Grained Measurements. *arXiv e-prints* arXiv:1601.02627 (2016). 1601.02627.
- [31] Kandala, A. *et al.* Hardware-efficient variational quantum eigensolver for small molecules and quantum magnets. *Nature* **549**, 242 EP – (2017).
- [32] Hempel, C. *et al.* Quantum chemistry calculations on a trapped-ion quantum simulator. *Phys. Rev. X* **8**, 031022 (2018).
- [33] Nam, Y. *et al.* Ground-state energy estimation of the water molecule on a trapped ion quantum computer. *arXiv e-prints* arXiv:1902.10171 (2019). 1902.10171.
- [34] Giovannetti, V., Lloyd, S. & Maccone, L. Advances in quantum metrology. *Nature Photonics* **5**, 222 EP – (2011).
- [35] Farhi, E., Goldstone, J. & Gutmann, S. A Quantum Approximate Optimization Algorithm Applied to a Bounded Occurrence Constraint Problem. *arXiv e-prints* arXiv:1412.6062 (2014). 1412.6062.
- [36] Wineland, D. *et al.* Experimental issues in coherent quantum-state manipulation of trapped atomic ions. *J. Res. Natl. Inst. Stand. Technol.* **103**, 259–328 (1998).
- [37] Olmschenk, S. *et al.* Manipulation and detection of a trapped  $\text{yb}^+$  hyperfine qubit. *Phys. Rev. A* **76**, 052314 (2007).
- [38] Brown, K. R., Harrow, A. W. & Chuang, I. L. Arbitrarily accurate composite pulse sequences. *Phys. Rev. A* **70**, 052318 (2004).
- [39] Sørensen, A. & Mølmer, K. Quantum computation with ions in thermal motion. *Phys. Rev. Lett.* **82**, 1971–1974 (1999).
- [40] James, D. F. V. Quantum dynamics of cold trapped ions with application to quantum computation. *Applied Physics B* **66**, 181 (1998).

## METHODS

### Quantum Approximate Optimization Algorithm (QAOA)

The QAOA is an approximate optimization algorithm first introduced in 2014 by Farhi *et al.* [5], and has since enjoyed growing interest. The QAOA uses alternating evolutions under two operators, typically a problem (or cost) Hamiltonian  $H_A$  that encodes the cost function on the diagonal in (say) the  $\sigma^x$  basis, and a transverse term  $H_B = -\sum_{i=0}^N \sigma_i^y$  that generates transitions between bit strings, such that the initial state  $|+\rangle_y^{\otimes n}$  evolves into an approximate ground state of  $H_A$ .

Practically, the most valuable feature of the QAOA seems to be its “learnability” via a classical outer loop optimizer, where the discovery of the evolution angles in the optimal QAOA schedule is achieved via the discovery

of structure in the angle sequences [13, 19, 20]. We show in this work that these patterns are seen quite generally across local Hamiltonian problems, and while steps towards a theory describing optimal QAOA sequences have been taken [19], several questions surrounding it remain open. Regardless, the structure in optimal QAOA schedules may be harnessed to implement state preparation in a scalable fashion and with a low overhead on quantum resources.

First, we discuss how to discover optimal QAOA1 schedules, i.e., QAOA schedules for  $p = 1$ .

#### QAOA, $p = 1$

Despite its apparent simplicity, the  $p = 1$  QAOA (or QAOA1) can be a powerful state preparation ansatz. For example, hardness-of-sampling results are known for QAOA1 circuits [14], closely mirroring the hardness of sampling from instantaneous quantum polynomial (IQP) circuits. Furthermore, it is known that the performance of the QAOA1 for certain combinatorial optimization problems can be competitive with the best classical algorithms for the same problems [35]. Another desirable feature of the QAOA1 for local spin Hamiltonians is the tractability of computing energy expectation values, as observed in [5]. A very similar result has also been known in the setting of quantum dynamics, [27]. For a two-local transverse field spin Hamiltonian as in Eq. 1, this leads to a formula for the energy expectation under a state produced by the QAOA1, starting from the product state  $|+\rangle^{\otimes N}$  (see Supplement for the result and derivation). These formulas are applicable to many cases of interest in quantum state preparation and optimization. Importantly, the time complexity to compute the formula is  $O(N^3)$  in the worst case, making it tractable to optimize the QAOA1 protocols for large spin chains.

#### QAOA, $p > 1$

The general analytical formula for  $p = 1$  does not extend to the case where we apply the QAOA for more than one layer. Here, we must turn to classical numerical methods to find the optimal QAOA angles  $\beta_i, \gamma_i$  for each layer  $i$ . For  $p$  layers, this is an optimization on a  $2p$ -dimensional space that grows exponentially with the depth of the circuit. However, numerics done here and in [13, 20] have identified the existence of minima that exhibit patterns in the optimal QAOA angles, namely that the angles, when plotted as a function of their index  $i$ , form smooth curves for any  $p$ . While this observation points to a deeper theoretical mechanism at play, it doesn't directly simplify the optimization problem, since we must still search over all approximately smooth sequences of the angles. Zhou *et al.* [13] have exploited

the smoothness of the functions by carrying out searches in the Fourier domain. Here, we follow a different route that arises from some novel observations of these family of minima.

For each  $p$ , denote the special optimal angles by  $\left\{ \left( \beta^{*(p)}, \gamma^{*(p)} \right) \right\}_p$ , which we can also think of as a pair of angle curves (as a function of step index  $i$ ). As  $p$  is varied, we may think of these minima as a family. We numerically find that this family exhibits the following desirable features (for  $p$  sufficiently large):

1. The angles are non-negative, small and bounded.
2. For  $p$  sufficiently large, the two angle sequences  $\beta^{*(p)}$  and  $\gamma^{*(p)}$  are approximately smooth.
3. The angle sequence  $\beta^{*(p)}$  (and correspondingly,  $\gamma^{*(p)}$ ) when viewed as a function on the normalized time parameter  $s_i = \frac{i-1}{p-1}$ , is convergent in the parameter  $p$ . In other words, as  $p$  is increased, the angle sequences  $\beta^{*(p)}$  and  $\gamma^{*(p)}$  approach a smooth, asymptotic curve (See Figure S1.)
4. The energy expectation  $E(\beta^{*(p)}, \gamma^{*(p)})$  approaches the global minimum as  $p \rightarrow \infty$ , and hence this family is asymptotically optimal.

The significance of the first point is that in experimental settings, large evolution times are infeasible to implement due to decoherence, so these minima correspond to practicable QAOA protocols. The third and fourth points suggest an inductive algorithm where a locally optimal schedule for a given  $p$  may be discovered using the optimal schedule for  $p - 1$  as a prior.

Point 3 in the above list is a novel observation that allows us to construct a heuristic that is efficiently scalable for large  $p$ . The main idea behind this construction is that the minimal angle curves for a larger  $p$  may be guessed from the optimal curve of a smaller  $p' < p$  by interpolation.

Utilizing the above points, we use a bootstrapping algorithm to find the optimal angle sequences,  $\beta^{*(p)}$  and  $\gamma^{*(p)}$ , for a given  $p$ , as described below. Let  $q = 1, \dots, p$  denote an intermediate angle index. Then:

1. For  $q = 1$ , use an analytic formula to find  $\beta^{*(1)}$  and  $\gamma^{*(1)}$ .
2. For  $q = 2$ , choose an initial guess of  $\beta^{(2)} = (\beta^{*(1)}, \beta^{*(1)} - 0.2)$  and  $\gamma^{(2)} = (\gamma^{*(1)}, \gamma^{*(1)} + 0.2)$ .
3. Perform a local optimization of  $\beta^{(2)}$  and  $\gamma^{(2)}$  in order to find  $\beta^{*(2)}$  and  $\gamma^{*(2)}$ .
4. Repeat the next steps (5-7) for  $q = 3, \dots, p$ .
5. Create interpolating functions through the angle sequences,  $\beta^{*(q-1)}$  and  $\gamma^{*(q-1)}$ , using the normalized time  $s_i = \frac{i-1}{q-2}$  as the independent parameter

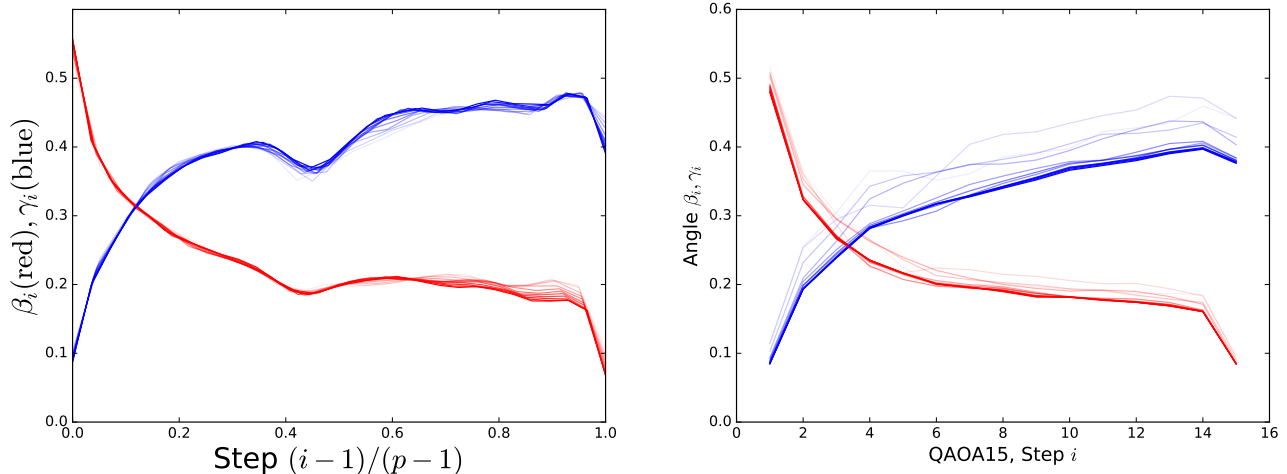


**Figure S1: Convergence in  $p$  and  $N$ .** Convergence of optimal angle curves with increasing QAOA layers  $p$  (left), and number of spins  $N$  (right). The  $p$ -convergence plot was generated for an  $N = 8$  spin system, for  $p$  ranging from 20 up to 30, with higher  $p$  shaded darker. The  $N$ -convergence figure was generated for a 15 layer QAOA, for  $N$  in the range of 4 to 14, with higher  $N$  curves shaded darker.

(we use a linear interpolation for  $q = 3$  and cubic for  $q > 3$ ).

6. Choose the initial guesses for  $\beta^{(q)}$  and  $\gamma^{(q)}$  by sampling the interpolating function from (5) at evenly spaced points separated by a normalized time distance of  $\Delta s = 1/(q-1)$ .
7. Perform a local optimization of  $\beta^{(q)}$  and  $\gamma^{(q)}$  in order to find  $\beta^{*(q)}$  and  $\gamma^{*(q)}$ .

The resulting angles  $\beta^{*(p)}$  and  $\gamma^{*(p)}$  should be at least a good local minimum of the energy expectation value and approaches the global minimum as  $p \rightarrow \infty$ .

The  $q = 2$  interpolation in step 2 is based on our observation that the  $\beta$  angles tend to curve down at the end and the  $\gamma$  angles tend to curve up.

An important feature of our algorithm is that its asymptotic runtime is expected to be efficient in  $p$ . This feature is predicated on the previous result that the angle curves are generally convergent as  $p$  tends to infinity. The argument proceeds as follows: if we assume a maximal deviation of the initial guess for layer  $q$  to be  $\epsilon_q \geq 0$ , then the total  $l_2$  distance between the initial guess and the optimized curve is no greater than  $\epsilon_q \sqrt{q}$ . Therefore, the local search algorithm is confined to a ball of radius at most  $\epsilon_q \sqrt{q}$ , and for a fixed error tolerance, the convergence time for a standard local optimizer is  $O(\epsilon_q^2 q)$ . Summing over convergence times for all from  $q = 1, \dots, p$ , we have

$$T = O\left(\sum_{q=1}^p q \epsilon_q^2\right) \leq O(p^2) \quad (6)$$

The last inequality above comes about as follows: while

the summand depends on the convergence rate of the sequence  $\{\epsilon_q\}_{q=1}^p$ , it is upper bounded by  $O(q)$  for a converging set of paths and an initial error  $\epsilon_1$  of order 1. The latter is true since our angle search domain is bounded and independent of  $N$ . Therefore, the sum is no greater than  $O(p^2)$ . In practice, even faster runtimes are possible. Therefore, the bootstrap algorithm exploits the structure of the special minima and provides a scalable route to multi-step QAOA for the long-range TFIM. In fact, as discussed in the supplement and in [19], there is mounting numerical evidence that the path approach applies across a very general variety of models on discrete as well as continuous systems.

#### Convergence in $N$

In the previous sections, we introduced a bootstrap algorithm that is asymptotically efficient in the number of layers  $p$ . However, in order to be fully scalable the algorithm must also be scalable in the system size  $N$ . This may not be possible in general (say for random spin models), as the optimized angles for a particular small system may have no bearing on the angles for a larger system. However, for the long-range TFIM, and indeed any translationally-invariant model with a well-defined notion of metric and dimension arising from the functional form of the coupling coefficients  $J_{ij}$ , it is reasonable to expect that the optimized angles depend on system size in a predictable way. This is indeed the case for the long-range TFIM. There, it can be seen that the angle curves for varying  $n$  appear similar in shape. Usefully, the curves also appear to be *convergent* to an ideal-



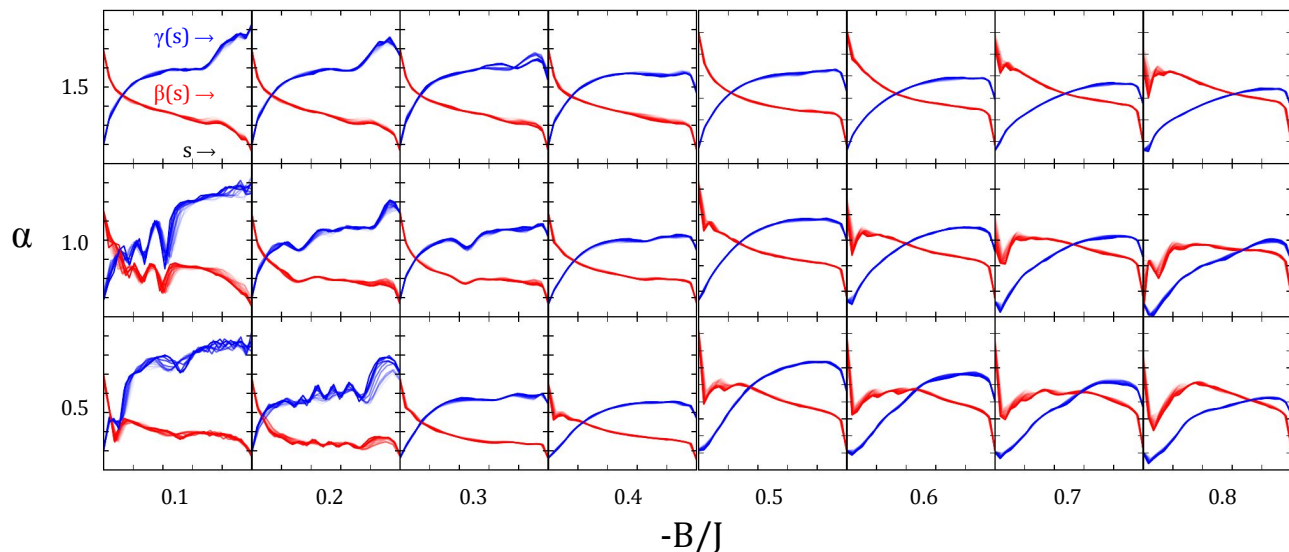


**Figure S2: Angle sequence curves.** A collage of angle sequence curves, arranged by the Hamiltonian parameters for which they were computed. In each box, the horizontal axis represents fractional step  $s = (i-1)/(p-1)$  ranging from 0 to 1, while the vertical axis gives the value of the angles  $\beta$  (red), and  $\gamma$  (blue). The subplots are arranged horizontally by  $-B/J_0$ , increasing from 0.1 to 0.8 in steps of 0.1 (from left to right), and vertically by the long-range power  $\alpha = 0.5, 1.0, 1.5$  (bottom to top). This collage shows the persistence of structure in the optimal angle sequences for a range of Hamiltonians within the same family.

ized curve for a hypothetical continuous, long-range spin chain. Once again, this feature suggests that the optimized QAOA angle curves for small systems may be used as initial guesses for larger systems *within the same Hamiltonian family*.

While it is not clear (due to numerical limitations) how fast the curves converge, we argue that the rate should be weakly dependent (or independent) of the system size  $N$ . For a given coupling function (such as inverse power-law) that decays as a function of distance, one may define a skin depth  $\delta$  that is the number of sites from the boundaries that the coupling is, say, a factor of  $e$  smaller than the nearest-neighbour value. Clearly,  $\delta$  is independent of the system size  $N$  and depends only on the parameters of the coupling function. For instance, for the long-range TFIM,  $\delta \sim e^{1/\alpha}$ . As  $N$  tends to infinity, the *fractional* skin depth  $\delta/N$  then “falls away” and becomes vanishing with respect to the bulk region of the chain. Now, we make the assumption that any deviations in the optimal QAOA schedules from  $N$  to  $N+1$  arise from change in the fractional skin depth, which is reasonable for a translationally invariant model. The incremental change in the fractional skin depth from  $N$  to  $N+1$  is  $\delta/N - \delta/(N+1) \sim O(1/N^2)$ . Therefore, if the change in the optimal QAOA curves  $\epsilon_N$  (in, say,  $l_1$  distance) is a smooth function of the fractional skin depth, then we expect it to vary as  $\epsilon_N \sim 1/\text{poly}(N)$ . Therefore, the total running time of a bootstrap from small system sizes to a given size  $n$  should be  $O\left(\sum_{k=1}^n 1/\text{poly}(N)\right)$  which is sub-linear in  $N$ . Combining this observation with the conver-

gence in  $p$ , we see that for a given Hamiltonian family, optimized QAOA angle curves for small  $p$  may be used as a rubric for the optimization for longer circuit depths. Furthermore, if the Hamiltonian is translationally-invariant with decaying interactions, the optimized QAOA schedules are expected to scale with  $N$  as well. Therefore, the state preparation procedure under the QAOA for such a Hamiltonian family is scalable in circuit “volume”, for a wide range of Hamiltonian parameters (Figure S2). This is our main theoretical contribution in this work.

### Evidence for hardness of sampling from general QAOA circuits

In this section we expand upon previous work [5] that gives evidence for exact sampling hardness of QAOA circuits, using the techniques of Refs. [28, 29] to give evidence for hardness of approximate sampling. First we relabel the bases  $Y \rightarrow X \rightarrow Z$  so that the  $p=1$  experiment is equivalent to preparing a state  $|\psi_0\rangle = |\uparrow\rangle_x^{\otimes N}$ , evolving under a Hamiltonian  $H_z$  diagonal in the computational basis, followed by a uniform rotation  $\tilde{H} = e^{-i\beta \sum_i \sigma_i^z}$  and measurement in the computational basis. Following Ref. [5], it suffices to consider QAOA circuits with  $\beta = \pi/4$ . The output state is  $\tilde{H}^{\otimes n} e^{-i\gamma H_z} H^{\otimes n} |0^n\rangle$  for some cost function  $C$  diagonal in the computational basis.

### Generalized gap of a function

The main idea behind proving exact sampling hardness is to examine a particular output amplitude, say the amplitude of the  $|0^n\rangle$  basis state. In Ref. [28], the output state after a so-called IQP circuit (which only differs from the one here in that the final rotation is a global Hadamard  $H^{\otimes n}$  instead of  $\tilde{H}^{\otimes n}$ ) has an amplitude proportional to a quantity known as the *gap* of a Boolean function,  $\text{gap}(f) = \sum_{x:f(x)=0} 1 - \sum_{x:f(x)=1} 1$ , the difference in the number of inputs that map to 1 and the number of inputs that map to 0 under  $f$ . Finding the gap of a general function is a **GapP**-complete problem. This is a very hard problem since the class **GapP** includes **#P**, which in turn includes the whole of **NP**. The authors of Ref. [28] prove that the gap of a degree-3 polynomial over  $\mathbb{Z}_2$ ,  $f$ , may be expressed as an output amplitude of an IQP circuit. They also show that the finding the gap of such functions  $f$  is still **GapP**-complete. Following Ref. [28], we examine the  $|0^n\rangle$  output amplitude of a QAOA state:

$$\langle 0^n | \tilde{H}^{\otimes n} e^{-i\gamma H_z} H^{\otimes n} | 0^n \rangle = \frac{1}{2^n} \sum_{x,y} \langle y | i^{\sum_i y_i + \tilde{f}(x)} | x \rangle, \quad (7)$$

where now we define the function  $\tilde{f}$  to have the range  $\mathbb{Z}_4$  and the Hamiltonian  $H_z$  satisfies  $e^{-i\gamma H_z} |x\rangle = i^{\tilde{f}(x)} |x\rangle$  for a computational basis state  $|x\rangle$ . The output amplitude is thus proportional to a ‘generalized gap’  $\text{ggap}(f) := \sum_{x:f(x)=0} 1 + i \sum_{x:f(x)=1} 1 + i^2 \sum_{x:f(x)=2} 1 + i^3 \sum_{x:f(x)=3} 1$  of a function  $f(x) = \tilde{f}(x) + \text{wt}(x)$ , where  $\text{wt}(x)$  is the Hamming weight of  $x$ . This modified function  $f(x)$  is also a degree-3 polynomial over  $\mathbb{Z}_4$ . Note that this restriction to degree-3 comes from the fact that the gates  $Z$ ,  $CZ$  and  $CCZ$  are universal for classical computation (indeed, the Toffoli alone is universal for classical computation) and there is a natural degree-3 polynomial coming from this construction. The quantity we have defined,  $\text{ggap}(f)$ , can be easily shown to be **GapP**-hard to compute, by reducing  $\text{gap}$  to  $\text{ggap}$ . This suffices for exact sampling hardness assuming the polynomial hierarchy (PH) does not collapse.

### Approximate sampling hardness

For approximate sampling hardness, we need two other properties, namely anti-concentration and a worst-to-average case reduction. Anti-concentration of a circuit roughly says that the output probability is sufficiently spread out among all possible outcomes so that not many output probabilities are too small. We choose a random family of QAOA circuits by choosing  $H_z$  such that the function  $f(x)$  is a degree-3 polynomial  $\sum_{i,j,k} a_{i,j,k} x_i x_j x_k + \sum_{i,j} b_{i,j} x_i x_j + \sum_i c_i x_i$  with

uniformly random weights  $b_{i,j}$  and  $c_i \in \mathbb{Z}_4$ . Anti-concentration then follows from the Paley-Zygmund inequality and Lemma 4 of the Supplemental Material of Ref. [28] (with  $r = s = 4$ ).

Finally, we need to show that the problem of approximating the generalized gap is average-case hard. Currently, no scheme for quantum computational supremacy has achieved this, and the best known result in this direction is in Ref. [29], where the authors show a worst-to-average case reduction for the problem of *exactly* computing an output probability of a random quantum circuit. The authors remark that their techniques may be extended to any distribution parametrized by a continuous variable. In principle, we have such a parameter  $\gamma$  available here, which continuously changes the parameters  $b_{i,j}$  and  $c_i$ . However, we have only shown anti-concentration when the weights  $b_{i,j}$  and  $c_i$  are chosen from a finite set. It remains to be seen whether one can have the property of anti-concentration and average-case hardness holding at the same time for some specific QAOA output distribution.

### Trapped-ion experimental systems

In this work two quantum simulators have been used, referred to as system 1 and 2. System 1 [23] is a room-temperature ion-trap apparatus, consisting of a 3-layer linear Paul trap with transverse center-of-mass motional frequency  $\nu_{\text{COM}} = 4.7$  MHz and axial center-of-mass frequencies  $\nu_x$  ranging from 0.39 to 0.6 MHz depending on the number of trapped ions. In this system Langevin collisions with the residual background gas in the ultra high vacuum (UHV) apparatus are the main limitation to ion chain lifetime [36]. These events can melt the crystal and eject the ions from the trap because of rf-heating or other mechanisms.

System 2 [24] is a cryogenic ion-trap apparatus based on a linear blade trap with four segmented gold coated electrodes. The trap is held at 6.5 K in a closed cycle cryostat, where differential cryo-pumping reduces the background pressure at low  $10^{-12}$  Torr level, which allows for long storage times of large ion chains. For this reason system 2 has been used to perform the QAOA with a large number of qubits (Fig. 2b) or when a large number of measurements was required (Fig. 4). The two transverse trap frequencies are  $\nu_{\text{COM}}^y = 4.4$  MHz and  $\nu_{\text{COM}}^z = 4.26$  MHz, and the axial frequency ranges from 0.27 to 0.46 MHz.

### State preparation

The qubit is initialized by applying resonant 369.5 nm light for about 20  $\mu\text{s}$  to optically pump into the  $|\downarrow\rangle_z$  state. To perform global rotations in the Bloch

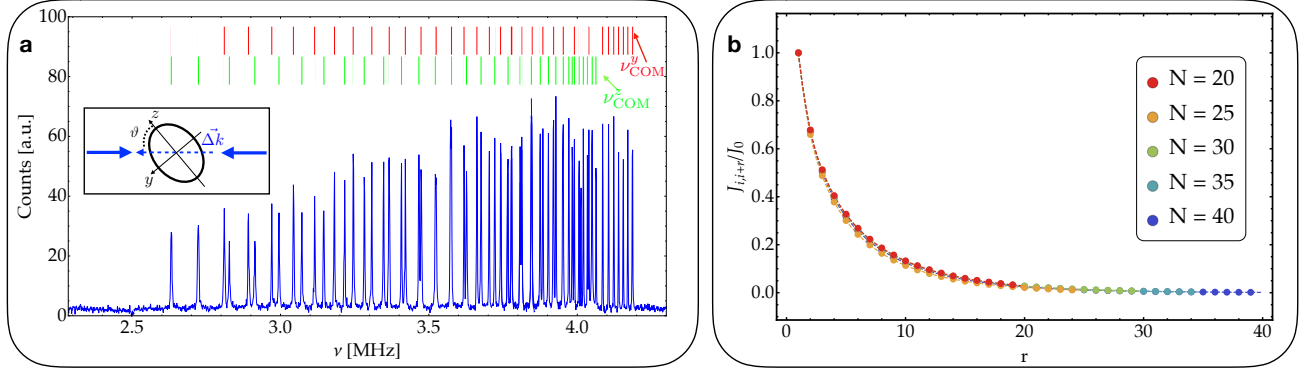


**Figure S3: System 2 characterization.** (a) Sideband resolved spectroscopy of a 32 ion chain with frequencies  $\nu_{COM}^y = 4.18$  MHz and  $\nu_{COM}^z = 4.06$  MHz, with both radial families identified. Inset: geometrical configuration of the global Raman beams (blue arrows) with respect to the transverse principal axes of the trap (black arrows). The ellipsoid shows qualitatively an equipotential surface of the trap. (b) Average spin-spin interaction matrix element  $J_{i,i+r}$  as a function of ion separation  $r = |i - j|$  for the data taken in Fig. 2c, calculated with the system parameters directly measured with sideband spectroscopy. The results are normalized to the average nearest-neighbour coupling  $J_0$  for each system size.

sphere, we apply two far-detuned, non-copropagating Raman beams whose beatnote is tuned to the hyperfine splitting  $\nu_0 = 12.642821$  GHz of the clock states  $^2S_{1/2}|F = 0, m_F = 0\rangle$  and  $^2S_{1/2}|F = 1, m_F = 0\rangle$  encoding the qubit [37]. State preparation in our implementation of the QAOA requires qubit initialization in the  $|\downarrow\rangle_z$  state by optically pumping the ions and then a global rotation into the  $|\uparrow\rangle_y$  state using stimulated Raman transitions. We detect the state of each ion at the end of each experimental sequence using state-dependent fluorescence, with single site resolution. In order to improve the accuracy of global qubit rotations, we employ a composite pulse sequence based on the dynamical decoupling BB1 scheme [38]. This allows us to compensate for inhomogeneity due to the Raman beam's Gaussian profile and achieve nearly 99% state preparation fidelity. The BB1 four pulse sequence is:

$$U_1(\pi/2) = e^{-i\frac{\pi}{2}\sigma_i^y} e^{-i\pi\sigma_i^z} e^{-i\frac{\pi}{2}\sigma_i^y} e^{-i\frac{\pi}{4}\sigma_i^x},$$

where after the first  $\pi/2$  rotation  $e^{-i\frac{\pi}{4}\sigma_i^x}$ , three additional rotations are applied: a  $\pi$ -pulse along an angle  $\theta = \cos^{-1}(-1/16) = 93.6^\circ$ , a  $2\pi$ -pulse along  $3\theta$ , and another  $\pi$ -pulse along  $\theta$ . The axes of these additional rotations are in the  $x$ - $y$  plane of the Bloch sphere with the specified angle referenced to the  $x$ -axis.

### Generating the Ising Hamiltonian

We generate spin-spin interactions by employing a spin dependent force with a pair of non-copropagating 355 nm Raman beams, with a wavevector difference  $\Delta k$  aligned along the transverse motional modes of the ion chain. The two off-resonant Raman beams are controlled using acousto-optic modulators which generate two inter-

ference beatnotes at frequencies  $\nu_0 \pm \mu$  in the Mølmer-Sørensen configuration [39]. In the Lamb-Dicke regime, the laser-ion interaction gives rise to the effective spin-spin Hamiltonian in Eq. 1, where the coupling between the  $i$ -th and  $j$ -th ion is:

$$J_{ij} = \Omega^2 \nu_R \sum_m \frac{b_{im} b_{jm}}{\mu^2 - \nu_m^2}. \quad (8)$$

Here  $\Omega$  is the Rabi frequency,  $\nu_R = \hbar \Delta k^2 / (8\pi^2 M)$  is the recoil frequency,  $\nu_m$  is the frequency of the  $m$ -th normal mode,  $b_{im}$  is the eigenvector matrix element for the  $i$ -th ion's participation to the  $m$ -th normal mode ( $\sum_i |b_{im}|^2 = \sum_m |b_{im}|^2 = 1$ ) [40], and  $M$  is the mass of a single ion.

Differently from system 1, where the wavevector difference  $\Delta k$  of the Raman beams is aligned along a principal axis of the trap, in system 2 the spin-spin interaction stems from the off resonant coupling to both families of transverse normal modes. Eq. (8) is then generalized to:

$$J_{ij} = J_{ij}^y + J_{ij}^z$$

$$J_{ij}^\ell = \Omega_\ell^2 \nu_R^\ell \sum_m \frac{b_{im} b_{jm}}{\mu^2 - (\nu_m^\ell)^2}, \quad \ell = y, z \quad (9)$$

where  $\nu_R^\ell$  is the recoil frequency given by the projection of the Raman wavevector  $\Delta k$  along the two radial principal axes of the trap  $\ell = y, z$ . We infer an angle  $\vartheta \sim 50^\circ$  between  $\Delta k$  and the  $z$  principal axis (see inset in Fig. S3a) from the ratio between the spin-phonon couplings to the two radial center of mass modes. Before every experiment, we perform Raman sideband cooling on both the center-of-mass and the two nearby tilt modes for both transverse mode families.

As we scale up the number of qubits (see Fig. 2c in the main text), we vary the axial confinement in order to maintain a self-similar functional form of the spin-spin

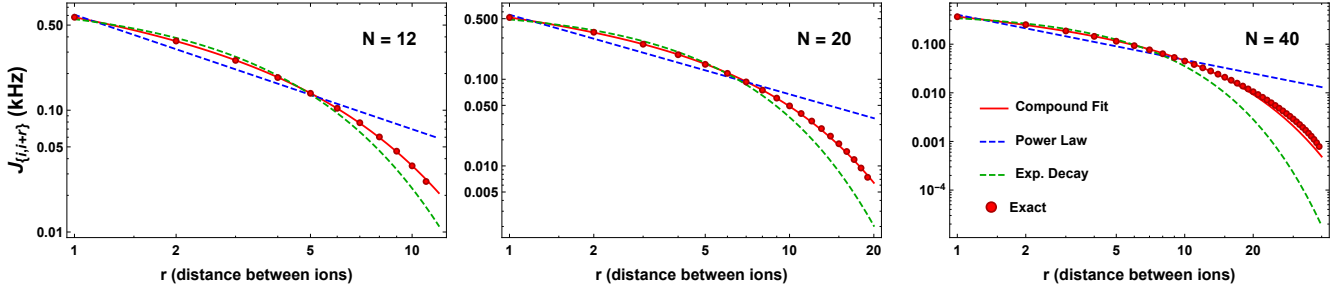


**Figure S4: Log-log plot of spin-spin interactions:** red points represent the average Ising couplings between spins separated by distance  $r = |i - j|$ , calculated from experimental parameters using Equation 8. These plots show the exact average couplings and fits corresponding to the  $N = 12$  and  $N = 20$  gradient descent experiments (Figure 3) and the  $N = 40$  exhaustive search experiment (Figure 2c). The power law fit (blue dashed curve) fails to match the couplings for larger spin separations, as does an exponential fit (green dashed curve). The compound formula (Equation 11) fits well the actual couplings for all spin separations, even for a chain of 40 ions. The fitted parameters  $\{J_0, \alpha', \beta'\}$  for  $N = 12, 20,$  and  $40$  are  $\{0.580, 0.322, 0.229\}$ ,  $\{0.517, 0.318, 0.181\}$ , and  $\{0.369, 0.383, 0.134\}$  respectively.

interaction (see Fig. S3b). For the data in Fig. 2c, we set the detuning to  $\delta = \mu - \omega_{COM}^y = 45$  kHz and the axial frequency to  $\nu_x = 0.46, 0.37, 0.36, 0.31, 0.27, 0.28$  MHz, for  $N = 20, 25, 30, 35, 40$  respectively.

#### Fitting Ising Couplings to Analytic Form

By directly measuring trap parameters and spin-phonon couplings, we can calculate the spin-spin interaction matrix  $J_{ij}$  with Eqs. (8) and (9). However, in order to efficiently compute the ground state energy of Hamiltonian (1) for  $N \gtrsim 25$  using DMRG, we approximate the Ising couplings using a translational invariant analytic function of the ion separation  $r = |i - j|$ . For  $N < 20$  the spin-spin coupling  $J_{ij}$  between the two qubits at distance  $r$  is well approximated by a power law decay:

$$J_{ij} \approx \frac{J_0}{r^\alpha} \quad (10)$$

where, as stated in the main text,  $J_0$  is the average nearest-neighbor coupling and  $\alpha$  is the power law exponent [25]. However for larger system sizes, this approximation fails to capture the actual decay of the interaction matrix.

In order to use the DMRG algorithm to accurately compute the ground state energies, we developed a compound function to better fit our couplings. This function is a product of a power law decay and an exponential decay parametrized by  $J_0, \alpha'$  and  $\beta'$ :

$$J_{ij} \approx \frac{J_0}{r^{\alpha'}} e^{-\beta'(r-1)} \quad (11)$$

As seen in Fig. S4, this functional form fits the exact Ising couplings well even for a chain of 40 ions, while both a power law and a pure exponential fit diverge significantly.

#### State Detection

We detect the ion spin state by globally rotating all the spins into the measurement basis with a composite BB1  $\frac{\pi}{2}$  pulse as described above, to rotate the  $x$  or  $y$  basis into the  $z$  basis, followed by the scattering of resonant laser radiation on the  ${}^2S_{1/2}|F=1\rangle \leftrightarrow {}^2P_{1/2}|F=0\rangle$  cycling transition (wavelength near 369.5 nm and radiative linewidth  $\gamma/2\pi \approx 20$  MHz). If the atom is projected in the  $|\uparrow\rangle_z$  “bright” state, it fluoresces strongly, while if projected in the  $|\downarrow\rangle_z$  “dark” state it fluoresces almost no photons because the laser is far from resonance [37].

In both systems the fluorescence of the ion chain is imaged onto an Electron Multiplying Charge Coupled Device (EMCCD) camera (Model Andor iXon Ultra 897) using an imaging objective with 0.4 numerical aperture and a magnification of 90x for both systems. The fluorescence of each ion covers roughly a 7x7 array of pixels on the EMCCD. After collecting the fluorescence for an integration time of 0.65 (1) ms for system 1 (2), we use a binary threshold to determine the state of each ion, discriminating the quantum state of each ion with near 98% (97%) accuracy in system 1 (2). The residual 2 (3)% errors include off-resonant optical pumping of the ion between spin states during detection as well as detector cross-talk between adjacent ions, readout noise, and background counts.

In system 2 the individual ion range-of-interests (ROIs) on the camera are updated with periodic diagnostic images, acquired by applying a nearly resonant cooling laser for 50 ms so that each ion fluoresces strongly regardless of its state. The signal to background noise ratio in the diagnostic shots is larger than 100, yielding precise knowledge of the ions’ center locations and taking into account the slow  $\sim 2\mu\text{m}$  pk-pk drift due to thermal expansion/contraction of the cryostat. Ion separations range from  $1.5\mu\text{m}$  to  $3.5\mu\text{m}$  depending on the trap settings and

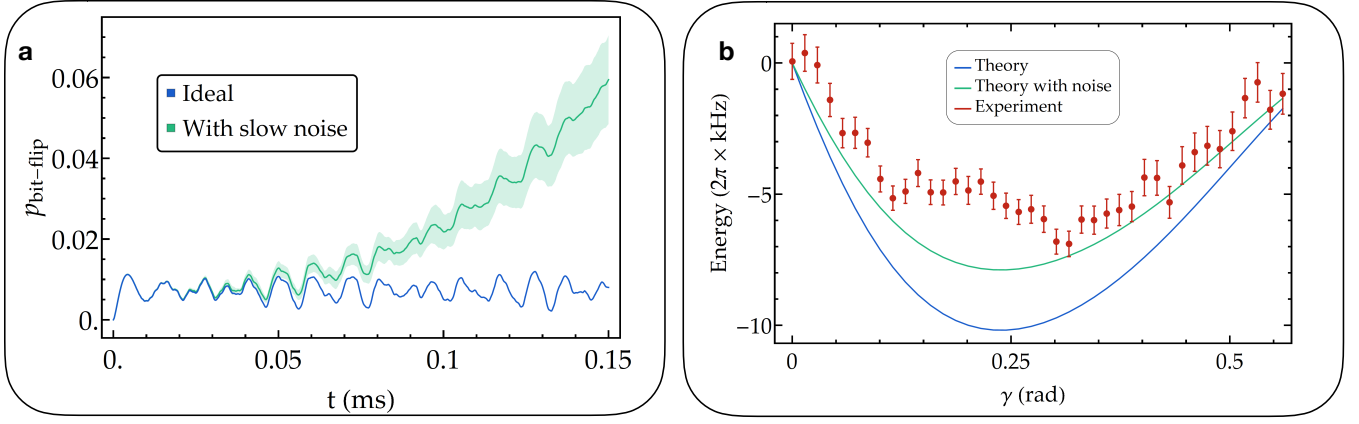


**Figure S5: Errors in trapped-ion quantum simulator:** (a) Phonon-assisted bit-flips per ion predicted by evolving the coherent off-resonant spin-phonon drive. The simulation includes slow drifts of the trap frequency and of the laser power over 440 shots, each including a Hamiltonian evolution of 0.15 ms, in a total time of 4 seconds. The shaded region is defined as the average  $p_i$  plus and minus one standard deviation (see main text for details). (b) Energy as a function of the  $\gamma$  parameter scan for Fig. 4 in the main text. Taking into account our total bit-flip error budget, we explain most of the discrepancy between our experimental performance and the ideal QAOA energy output.

the distance from the chain center, and are always much larger than the resolution limit of the diffraction-limited imaging system. We utilize the pre-determined ion centers to process the individual detection shots and optimize the integration area on the EMCCD camera to collect each ion’s fluorescence while minimizing cross-talk. We estimate cross-talk to be dominated by fluorescence from nearest-neighbor, which can cause a dark ion to be erroneously read as bright.

### Error sources

The fidelity of the quantum simulation is limited by experimental noise. A significant type of error that causes the system to depart from the ideal evolution is “bit-flip errors”. These errors are caused by off-resonant excitation of motional modes of the ion chain, which causes residual spin motion-entanglement. When the motion is traced out at the end of the measurement this results in an unwanted bit-flip. The probability of this error to occur on the  $i$ th ion [23] is proportional to  $p_i \sim \sum_{m=1}^N (\eta_{im}\Omega/\delta_m)^2$ , where  $\eta_{im} = b_{im}\sqrt{\nu_R/\nu_{COM}}$  (see Eq. 8) and  $\delta_m = \mu - \omega_m$  is the beatnote detuning from the  $m$ -th normal mode. We trade off a lower error for a weaker spin-spin coupling by choosing a  $\delta_{COM}$  such that  $(\eta_{COM}\Omega/\delta_{COM})^2 \lesssim 1/10$ . By considering all the off-resonant contributions of all the modes (see Fig. S5), we estimate the phonon error to cause about 1% bit-flip per ion. Additionally, this effect is amplified by fluctuations in the trap frequency and laser light intensity at the ions’ location, increasing the probability of a phonon-assisted bit-flip event. To take this into account, we included slow drifts and fluctuations of the trap fre-

quency and of the laser power on the timescale of 440 experimental repetitions assuming noise spectral density falling as  $1/f$ . Assuming a reasonable relative standard deviation  $\Delta\Omega/\Omega$  and  $\Delta\delta/\delta$  over the timescale required to average over quantum projection noise, we end up estimating an average bit-flip probability  $p_i \sim 5\%$  (see Fig. S5a). Another source of bit-flip errors is imperfect detection. Off-resonant pumping limits our average detection fidelity to 98%(97%) for system 1 (2). A detection error is equivalent to a random bit-flip event so the two errors will sum up.

Slow experimental drifts over the time scale of a few hours required for data-taking also cause averaging over different Ising Hamiltonian parameters. These fluctuations are related to laser light intensity noise at the ions’ location and drifts of the trap frequency. Other less important noise sources are related to off-resonant Raman scattering errors during the Ising evolution (estimated in  $7 \cdot 10^{-5}$  per ion) and RF heating of the transverse COM motional mode of the ion chain in system 1. A specific source of noise in system 2 is mechanical vibrations at 41 Hz and 39 Hz due to residual mechanical coupling to the cryostat. This is equivalent to phase-noise on the Raman beams, which leads to dephasing of the qubits.

In Fig. S5b, we plot the experimentally measured energy as a function of  $\gamma$ , and the corresponding theoretical curves with and without incorporating errors. Using the bit-flip probability  $p_i \sim 6\%$  estimated from our model considering phonons and detection errors, we get a better agreement with the experimental data, showing that we have a good understanding of the noise sources in our system.